Phytochemical Profiling and Anticancer Evaluation of Lantana camara Using Integrated Experimental and Computational Approaches

Banita Dhatwalia

banita.thakur1827@gmail.com

Chandigarh University

Stanley Arinze Abonyi

University of Nigeria

Neetu Sharma

Abhilashi University

Rashmi Kumari

Indira Gandhi National Open University

Research Article

Keywords: Lantana camara, LC-MS profiling, Anticancer activity, Network pharmacology, Molecular docking

Posted Date: March 23rd, 2026

DOI: https://doi.org/10.21203/rs.3.rs-8538940/v1

Additional Declarations: No competing interests reported.

Phytochemical Profiling and Anticancer Evaluation of *Lantana camara* Using Integrated Experimental and Computational Approaches

Banita Dhatwalia[1]*, Stanley Arinze Abonyi[2], Neetu Sharma[3], Rashmi Kumari[4]

[1*]Assistant Professor, University Centre of Research and Development (UCRD), Chandigarh University, Mohali-140413, Punjab, India.

[2]Research Scholar, Department of Pharmaceutical Sciences, University of Nigeria, Nsukka, Nigeria

[3]Associate Professor, Department of Zoology, Abhilashi University, Mandi, Himachal Pradesh, India

[4]Research Scholar, Discipline of Life Sciences, School of Sciences, Indira Gandhi National Open University, New Delhi-110068, India

Abstract

Natural products remain an indispensable source of structurally diverse bioactive molecules for anticancer drug discovery. Present study examines the antioxidant, anticancer, and molecular activity of *Lantana camara* leaf ethanolic extract (LCEE) in integrated LC-MS profiling, in vitro experiments, network pharmacology, molecular docking, and ADMET analysis related to BCL2-associated pathways in prostate (PC-3), lung (A549), liver (HepG2), breast (MCF-7), and oral (KB-3-1) cancer. LC-MS identified 18 phytochemicals, including beta-nicotinamide adenine dinucleotide hydrate (S3), beta-nicotinamide adenine dinucleotide oxidized form (S4), delphinidin-3-O-beta-glucopyranoside (S6), marein (S11), and nicotinamide hypoxanthine dinucleotide sodium salt (S13); in the previous study, LCEE demonstrated potent antioxidant activity via ABTS, DPPH, and H2O2 assays, alongside dose-dependent cytotoxicity with IC50 values of94.53 mg/mL (MCF-7); while in a continued current study dose-dependent cytotoxicity with IC50 values of 76.62 mg/mL (A549), 132.4 mg/mL (HepG2), 112.5 mg/mL (PC-3), and 85.7 mg/mL (KB-3-1), achieving 65-83% maximum inhibition. Network pharmacology identified 753 compound targets overlapping BCL2 genes and cancer transcriptomes forming PPI networks that were enriched in apoptosis regulation, proteostasis (HSP90AA1/HSP90AB1 hubs), lysosomal pathways (CTSD), and oncogenic signalling (EGFR, CASP3), and lead compounds with docking scores -13 kcal/mol (e.g., S4-HSP90AB1: -15.88 kcal/mol These results make *L. camara* phytochemicals multi-target BCL2 network modulators, making them a subject of activity-driven fractionation and in vivo validation of the development of anticancer leads.

Keywords: *Lantana camara*, LC-MS profiling, Anticancer activity, Network pharmacology, Molecular docking

Introduction

Cancer is a global problem as one of the major causes of morbidity and mortality, and it continues to be a significant burden to healthcare sectors all over the world, even with the

massive progress in early diagnosis and treatment methods [1]. The recent estimates by the International Agency of Research on Cancer (IARC) indicated the occurrence of about 20 million cases of cancer and a cancer death rate of 9.7 million cancer cases across the world in 2022. The pressure is expected to launch with projections by the World Health Organization of more than 35 million additional cancer cases by 2050 signifying a 77 percent rise in comparison to the 2022 estimates [2]. The loss of control over programmed cell death is one of the primary cancer evolution characteristics that allow cancerous cells to avoid apoptosis and develop resistance to traditional treatment methods. The B-cell lymphoma 2 (BCL2) family of proteins is one of the essential molecular regulators of the intrinsic apoptotic pathway and helps to regulate the permeabilization of the outer membrane of the mitochondrion and caspase activation [3]. Anti-apoptotic BCL2 protein overexpression is also widely documented in numerous solid tumors, such as breast, lung, liver, prostate, oral cancer, among others, and it is associated with tumor survival, tumor chemoresistance, and poor clinical outcome. As a result of these studies, novel therapeutic targeting methods based on the regulation of BCL2-controlled signaling pathways have become an attractive drug discovery approach in the modern anticancer field [4].

Natural products have long been a rich and invaluable source of anticancer agents, both due to their remarkable chemical diversity, structural complexity, and their capacity to engage several molecular targets at a time [5]. The alkaloids, flavonoids, phenolics, and terpenoids derived by the plants have shown considerable anticancer properties that manipulate the process of apoptosis, cellular cycle, oxidative, and signal transduction [6-9]. Compared to the single-target synthetic drugs, the phytochemicals frequently have multitarget effects, which is particularly appealing towards the complex and heterogeneous cancer. Nevertheless, the molecular processes underlying the anticancer action of medicinal plants is a significant unexplored challenge, and a major challenge has been to function at the systems level by integrating both experimental validation and computational analysis approaches [10].

Lantana camara L. (Verbenaceae) is a common medicinal plant that is commonly used in the treatment of various ailments like inflammatory, microbial infections and tumors [11]. The studies of *L. camara* phytochemistry have shown the occurrence of a variety of secondary metabolites including: flavonoids, triterpenoids, phenolic acids and essential oils with some of them having been implicated in cytotoxic and pro-apoptotic activity [12,13]. Although these properties have good potential, the extensive mechanistic research on the association of the phytochemical profile of *L. camara* with particular molecular targets and cellular signaling pathways in cancer pathogenesis is scarce.

New developments in network pharmacology have equipped potent means to study complex relationships amid bioactive compounds, molecular targets, and pathways related to disease in a holistic system [14]. Network pharmacology can be used to systematically understand the mechanism of action of natural products through the use of phytochemical profiling, predicting targets, protein-protein interaction analysis, and pathway enrichment [15]. This method together with molecular docking, binding free-energy calculation and in silico ADMET profiling provides a powerful platform to identify possible lead compounds and confirm their molecular pharmacological relevance [16,17].

The current study will utilize a multi-disciplinary research design that includes experimental and computational studies to direct the investigation on the antioxidant and anticancer properties of *L. camara* leaf ethanolic extract (LCEE). In particular, the research will attempt to: Carry out LC-MS-based phytochemical profiling to determine and describe bioactive compounds in LCEE in both positive and negative ionization. Measure in vitro cytotoxicity (MTT assay) of the major cancer types in five human cancer cell lines (MCF-7 breast cancer, A549 lung cancer, HepG2 Liver cancer, PC-3 Prostate cancer and KB-3-1 oral cancer). Construct-compound-target-pathway networks between LCEE phytochemicals and BCL2-regulated apoptotic pathways by target prediction, PPI network analysis, and Gene Ontology enrichment. Find hub genes (e.g. HSP90, CASP3, EGFR, BCL2) that are high-confidence drug targets across cancer models. Perform molecular docking simulations and MM-GBSA binding energy calculations to predict lead compounds and their binding interactions with target proteins. Conduct ADMET profiling to assess pharmacokinetic and toxicity properties critical for drug-likeness and development feasibility

Methodology

Collection of plant

Leaves of LC were gathered from the Hamirpur district in Himachal Pradesh, where they are locally referred to as "Phulnu." Subsequently, the leaves were cleaned and left to dry in a shaded location. The dried leaves were then crushed and grind in a green fine powder with the help of mortar and pestle.[18]

Preparation of Ethanolic Extract

50 g of dried *Lantana camara* leaf powder was extracted with 500 mL of 80% ethanol (v/v) at 60°C for 6 h using a water bath with continuous stirring. The extract was filtered through Whatman No. 1 filter paper, concentrated under reduced pressure using a rotary evaporator at 45°C, lyophilized, and stored at 4°C. The yield was 8.2% (w/w). The lyophilized extract (LCEE) was dissolved in DMSO (final concentration <0.1%) for biological assays. [19]

Qualitative analysis of phytochemicals

For the phytochemical screening of LCEE the extract was examined for the presence of cabohydrates, tannins, phenols, alkaloids, saponins, flavonoids, terpenoids, glycosides, fats and oils. [20,21]

Anticancer activity

Cell Culture and MTT assay

All the 5 cell lines were acquired from NCCS (National Centre for Cell Sciences) in Pune. The culturing of cells and MTT assay was done by using the procedures followed by Dhatwalia and Sharma; 2024 and in the end, images were taken using an inverted microscope (Olympus ek2) with a camera (AmScope digital camera 10 MP Aptima CMOS). [22]

Statistical Analysis

All experiments were performed in triplicate (n=3). Data are presented as mean ± standard deviation (SD). IC50 values were calculated using non-linear regression in GraphPad Prism v6.0. Differences between treatments were analyzed by one-way ANOVA followed by Dunnett's post-hoc test. Statistical significance was set at $p<0.05$. [23]

LCMS Methodology

Phytochemical profiling of the plant extracts was performed using a liquid chromatography–tandem mass spectrometry (LC–MS/MS) system (Waters Alliance e2695 HPLC system coupled with a TQD mass spectrometer; model ACQ-TQD#QBB1152). The analysis was carried out following the procedure described by Dhatwalia and Sharma (2024). 10 mg of sample was dissolved in 1 ml methanol in a vial and vial was loaded in the instrument of sample acquisition. [24]

Chromatographic separation was achieved using a SUNFIRE C18 column (250 × 2.1 mm, 2.6 µm particle size) maintained at 35 °C. The mobile phase consisted of solvent A (acetonitrile) and solvent B (5 mM ammonium formate buffer). The elution was performed using a gradient program as follows: 0 min, 5% A; 25 min, 20% A; 40 min, 20% A; 55 min, 35% A; and 65 min, 80% A. The flow rate was maintained at 0.2 mL min^{-1}, and detection was carried out at 280 nm. The total run time was 40 min with a system pressure range of 0–300 bar.

For reproducibility validation, an additional gradient program was applied using the same analytical column and flow rate. The mobile phase comprised: A (H_2O), B (acetonitrile), C (methanol), and D (5 mM ammonium acetate). The gradient conditions were as follows: 1.00 min, 0%A/5%B/0%C/95%D; 10.00 min, 0%A/30%B/0%C/70%D; 16.00 min, 0%A/60%B/0%C/40%D; 24.00 min, 0%A/80%B/0%C/20%D; 32.00 min, 0%A/80%B/0%C/20%D; 35.00 min, 0%A/5%B/0%C/95%D; and 40.00 min, 0%A/5%B/0%C/95%D.

Phytochemical extracts served as the test samples, and all analyses were performed under standardized LC–MS/MS conditions to ensure peak reproducibility and accurate retention profiling. Spectra were recorded in negative and positive ionization mode between m/z 150 and 2000.

Online Data Bank: https://massbank.eu/MassBank/Search

Phytochemical Identification and Target Prediction

Phytochemicals detected from *Lantana camara* via LC–MS/MS profiling (positive and negative ionization modes) were identified using the PubChem database (https://pubchem.ncbi.nlm.nih.gov/)[25]. SMILES structures for each identified compound were retrieved and submitted to SwissTargetPrediction (http://www.swisstargetprediction.ch/)[26] to predict human protein targets. All predicted targets with non-zero probability scores were retained for downstream analysis.

Retrieval of Cancer-Associated Genes

Cancer-specific gene expression data were obtained from the DepMap database (https://depmap.org/portal/; release 25Q2). Expression profiles from five cancer cell lines were extracted: PC-3 (prostate, DepMap ID: ACH-000901), A549 (lung, ACH-000681), HepG2 (liver, ACH-000739), and MCF-7 (Luminal A breast, ACH-000019). The top 500 protein-coding genes ranked by transcript abundance (TPM) were selected for each cell line. For oral cancer, gene data were sourced from GeneCards (https://www.genecards.org/)[27] using the search term "oral cancer," with the top 500 genes ranked by relevance score included for analysis.

Network Construction and Enrichment Analysis

Overlapping gene targets between *Lantana*-derived compounds, BCL2-related compounds, and cancer-associated genes were identified using the Venn Diagram Online Tool v2.1.0 (https://bioinfogp.cnb.csic.es/tools/venny/index.html). These intersecting targets were used to construct a protein–protein interaction (PPI) network in the STRING database (https://string-db.org/)[28] with *Homo sapiens* as the organism and a minimum interaction score of 0.4 (medium confidence). Hub genes were identified using Cytoscape v3.10.4 [29]. Functional enrichment analysis, including Gene Ontology (Biological Process, Cellular Component, Molecular Function) and pathway enrichment, was performed using ShinyGO v0.85.1 (https://bioinformatics.sdstate.edu/go/) [30]. A comprehensive compound–target–pathway network was constructed in Cytoscape to visualize multi-target interactions within cancer-related apoptotic pathways.

ADMET Profiling

Pharmacokinetic and toxicity properties of *Lantana*-derived phytochemicals were predicted using ADMETLab 3.0 (https://admetlab3.scbdd.com/) [31]. SMILES structures from PubChem were input for analysis. Parameters evaluated included absorption (P-glycoprotein inhibition, human intestinal absorption, Caco-2 permeability), distribution (plasma protein binding, volume of distribution, blood–brain barrier penetration), metabolism (CYP3A4 and CYP2C9 inhibition, human liver microsomal stability), excretion (plasma clearance, half-life), and toxicity (hERG potassium channel inhibition).

Molecular Docking and Validation

Three-dimensional crystallographic structures of hub gene-encoded proteins were retrieved from the Protein Data Bank (https://www.rcsb.org/) with the following criteria: resolution ≤2.5 Å, presence of a co-crystallized ligand, and no mutations. Protein preparation was performed in Maestro (Schrödinger Suite v12.8) using the Protein Preparation Wizard, including bond order correction, hydrogen addition, removal of crystallographic water molecules within 5 Å of co-ligands, side chain/loop repair, pH-dependent protonation, and energy minimization with the OPLS3e force field. Molecular docking was conducted using Glide in Extra Precision (XP) mode [32]. All *Lantana* phytochemicals were docked into target protein binding pockets. Protocol validation was performed by redocking the native co-crystallized ligand of the highest-scoring protein–ligand complex using identical XP parameters; RMSD comparison

confirmed docking reliability. 3D visualization was performed using PyMOL, and 2D interaction diagrams were generated in Maestro.

Binding Free Energy Estimation (MM-GBSA)

Binding free energies of the top-ranked ligand–protein complexes were estimated using Molecular Mechanics/Generalized Born Surface Area (MM-GBSA) analysis. The binding free energy (ΔG_bind) was calculated using the equation:

$$\Delta G_{\text{bind}} = G_{\text{complex}} - (G_{\text{protein}} + G_{\text{ligand}})$$

where G_{complex} is the free energy of the receptor–ligand complex, G_{protein} is the free energy of the protein, and G_{ligand} is the free energy of the free ligand [33].

Results and Discussion

LC-MS Phytochemical Profiling

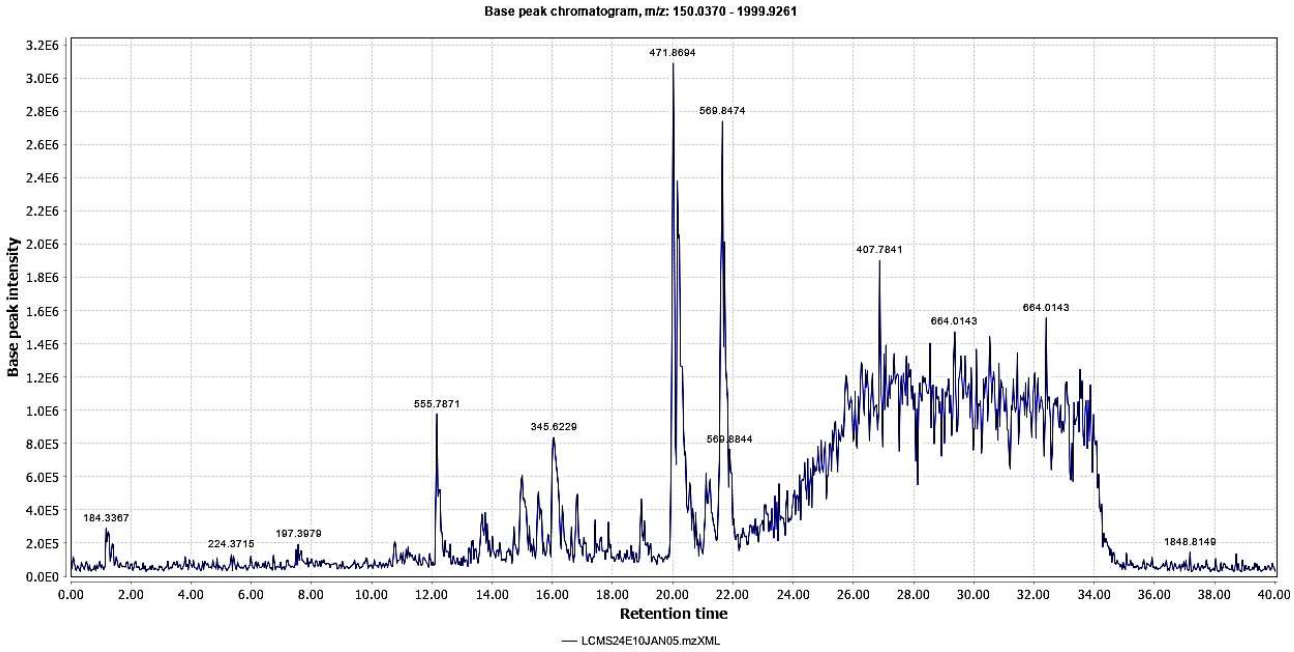

Graph 1: Total Ion Chromatogram (Positive Mode)

Table 1: Total Ion Chromatogram of LCEE (Positive Mode)

R. Time	Score	Compound Name	Ion	Formula	Exact Mass	Observed Mass	Mass Diff
1.18	0.859	L-Tyrosine	Positive	$C_9H_{11}NO_3$	181.073	184.3367	-3.2637
13.67	0.516	Delphinidin-3-O-Beta-Glucopyranoside	Positive	$C_{21}H_{21}O_{12}$	465.103	467.6884	-2.5854
13.77	0.514	(+-)-Alpha-Tocopherol Acetateacid Ester	Positive	$C_{31}H_{52}O_3$	472.391	469.7604	2.6306
15.00	0.906	Safranine	Positive	$C_{20}H_{19}N_4$	315.16	315.5413	-0.3813
15.55	0.773	Fusaric Acid	Positive	$C_{10}H_{13}NO_2$	179.094	177.4915	1.6025
16.06	0.795	Guanosine-3',5'-Cyclic Monophosphate	Positive	$C_{10}H_{12}N_5O_7P$	345.047	345.6229	-0.5759
18.96	0.744	Adenosine-3',5'-Cyclicmonophosphate	[M+H]+	$C_{10}H_{12}N_5O_6P$	329.21	329.5646	-0.3546

21.11	0.448	Zeaxanthin	Positive	$C_{40}H_{56}O_2$	568.428	569.9584	-1.5304
21.65	0.618	Canthaxanthin	Positive	$C_{40}H_{52}O_2$	564.396	569.8474	-5.4514
21.89	0.687	N-Stearoyl-D-Erythro-Sphingosine	Positive	$C_{36}H_{71}NO_3$	565.543	569.8844	-4.3414
25.75	0.234	Beta-Nicotinamide Adenine Dinucleotide Oxidized Form	[M+H]+	$C_{21}H_{28}N_7O_{14}P_2$	664.43	663.9773	0.4527
26.88	0.566	Leucylleucyltyrosine	Positive	$C_{21}H_{33}N_3O_5$	407.242	407.7841	-0.5421
29.37	0.641	Nicotinamide Hypoxanthine Dinucleotide Sodium Salt	Positive	$C_{21}H_{27}N_6O_{15}P_2$	665.1	664.0143	1.0857
32.41	0.483	Beta-Nicotinamide Adenine Dinucleotide Hydrate	Positive	$C_{21}H_{28}N_7O_{14}P_2$	664.116	664.0143	0.1017

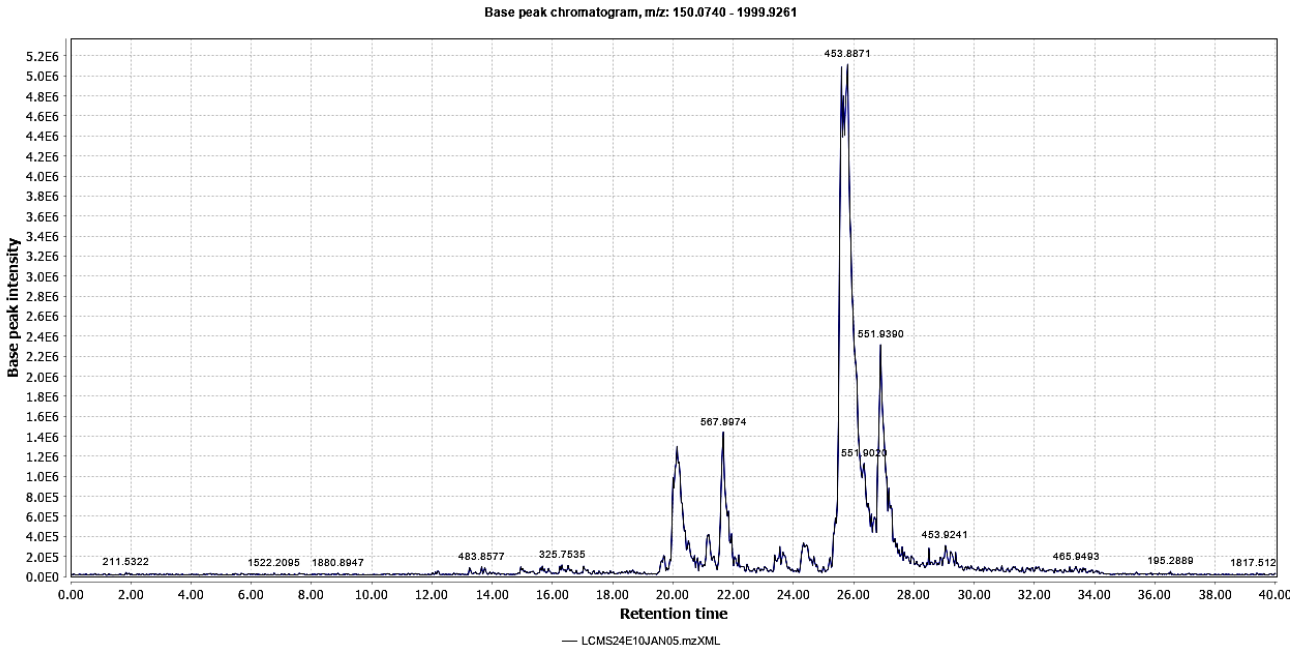

Graph 2: Total Ion Chromatogram (Negative Mode)

Table 2: Total Ion Chromatogram of LCEE (Negative Mode)

R. Time	Score	Compound Name	Ion	Formula	Exact Mass	Observed Mass	Mass Diff
25.60	0.895	Myricetin-3-Xyloside	Negative	$C_{20}H_{18}O_{12}$	450.079	453.8871	-3.8081
25.80	0.923	Marein	Negative	$C_{21}H_{22}O_{11}$	450.116	453.8871	-3.7711
26.35	0.686	UDP-Beta-L-Rhamnose	Negative	$C_{15}H_{24}N_2O_{16}P_2$	550.06	551.9020	-1.842
27.17	0.707	UDP-Beta-L-Rhamnose	Negative	$C_{15}H_{24}N_2O_{16}P_2$	550.06	551.9390	-1.879

LC-MS/MS analysis of *Lantana camara* ethanolic leaf extract (LCEE) identified a total of 18 phytochemicals across positive ionization mode (14 compounds) and negative ionization mode (4 compounds). The compounds were identified with high mass accuracy and characterized by retention times ranging from 1.18 to 32.41 minutes. Key phytochemicals identified included β-nicotinamide adenine dinucleotide hydrate (S3), β-nicotinamide adenine dinucleotide oxidized form (S4), delphinidin-3-O-β-glucopyranoside (S6), marein (S11), and nicotinamide hypoxanthine dinucleotide sodium salt (S13). All identified compounds were retrieved from PubChem and assigned unique identifiers (S1–S17) for downstream computational analyses.

In Vitro Cytotoxicity Evaluation

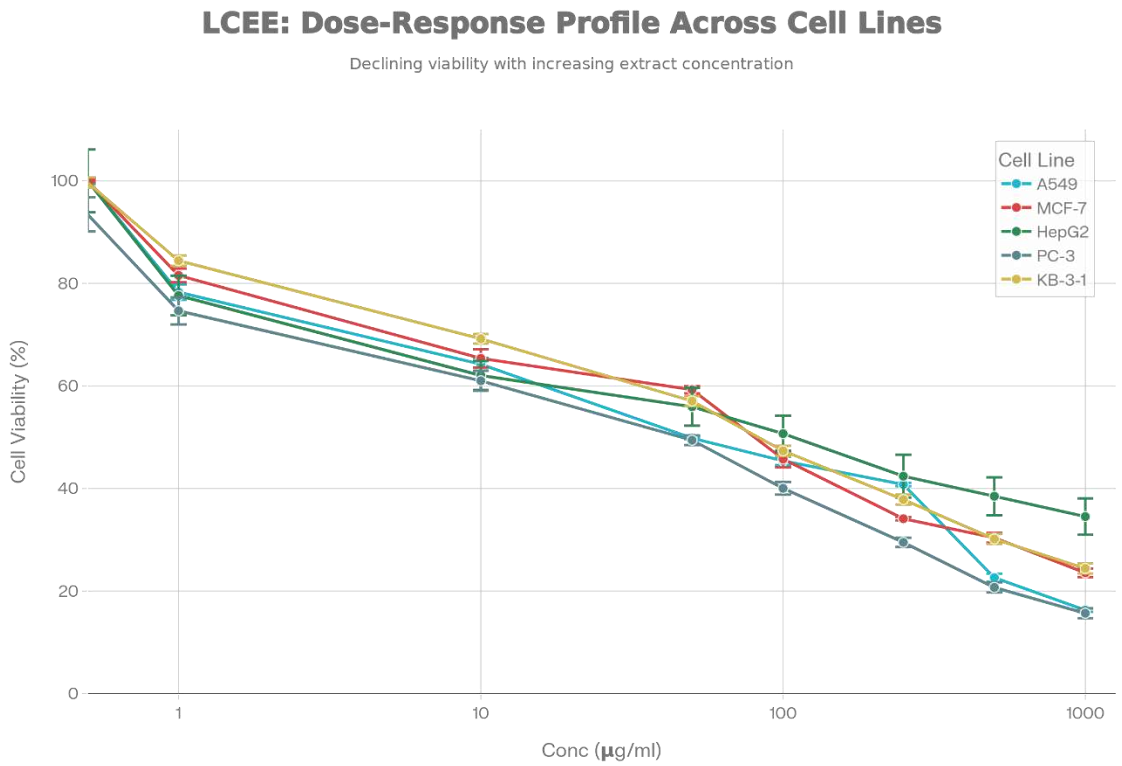

Graph 3. LCEE Dose-Response Profile Across Cell Lines. Line graph showing cell viability percentage at increasing LCEE concentrations across five cancer cell lines. Data points represent mean values with error bars indicating standard error of mean (SEM, n=4).

Table 1: LCEE Summary Statistics Across Cell Lines

Cell Line	IC50 (µg/ml)	Max Inhibition (%)	Conc. Range (µg/ml)	Activity
A549	76.62	83.7	0-1000	Highly Active
MCF-7	94.53	76.4	0-1000	Highly Active
HepG2	132.4	65.5	0-1000	Active
PC-3	112.5	83.3	0-1000	Highly Active
KB-3-1	85.7	75.6	0-1000	Highly Active

LCEE demonstrated dose-dependent cytotoxic activity against five cancer cell lines, with half-maximal inhibitory concentrations (IC_{50}) varying by cell line and cancer type. Specifically, A549 (lung cancer) showed the lowest IC_{50} of 76.62 µg/mL with 83.7% maximum inhibition, followed by KB-3-1 (oral cancer, 85.7 µg/mL, 75.6% inhibition) and MCF-7 (breast cancer, 94.53 µg/mL, 76.4% inhibition). PC-3 (prostate cancer) exhibited an IC_{50} of 112.5 µg/mL with 83.3% maximum inhibition, while HepG2 (liver cancer) showed the highest IC_{50} of 132.4 µg/mL with 65.5% maximum inhibition. All experiments were conducted in triplicate (n=4), with data presented as mean ± SEM. Differences between treatments were analyzed using one-

way ANOVA followed by Dunnett's post-hoc test, with statistical significance set at $p<0.05$. The concentration range tested for all cell lines was 0–1000 µg/mL, and all five cancer models were classified as either "Highly Active" (A549, MCF-7, PC-3, KB-3-1) or "Active" (HepG2) based on maximum inhibition percentages exceeding 65%.

Network Pharmacology Workflow and Target Identification

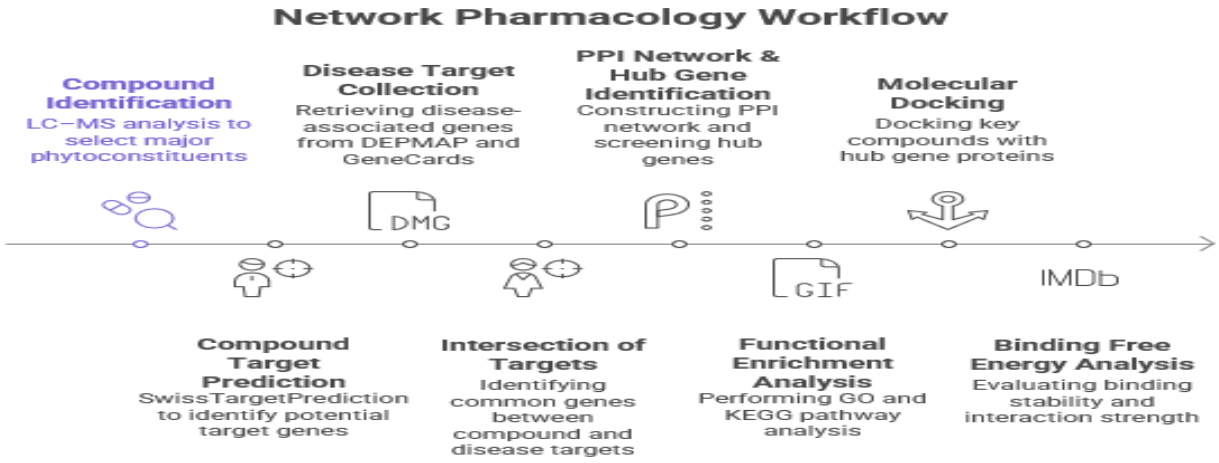

Figure 1. Network Pharmacology workflow.

To elucidate the potential anticancer mechanisms of LCEE phytochemicals at the systems level, an integrated network pharmacology framework was employed. SwissTargetPrediction analysis of the 18 LCEE-derived phytochemicals yielded a total of 753 compound-associated protein targets. These targets were integrated with 2000 BCL2-associated genes retrieved from GeneCards (based on relevance ranking) and the top 500 protein-coding genes from each of five cancer cell lines extracted from the DepMap 25Q2 dataset. For each cancer type, genes were ranked by transcript abundance (TPM), and the top 500 most highly expressed genes were selected to represent the major transcriptionally active drivers. This approach generated a comprehensive molecular interface linking LCEE phytochemicals to BCL2-regulated apoptotic pathways across prostate (PC-3), lung (A549), liver (HepG2), breast—Luminal A subtype (MCF-7), and oral (KB-3-1) cancers.

Venn Diagram Analysis and Intersection Targets

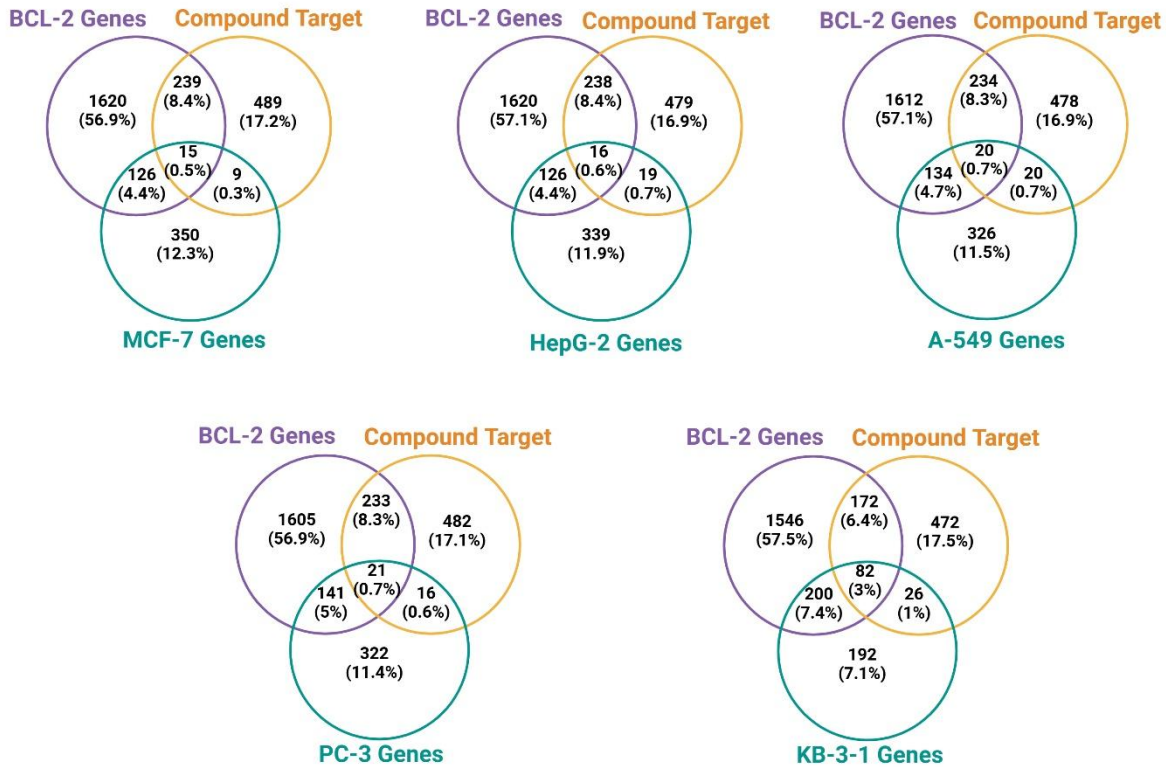

Figure 2: Venn diagram showing the intersection of target genes of *Lantana camara* extract, BCL2 related targets and cancer targets.

Intersection analyses were conducted to identify overlapping gene targets among three datasets: LCEE-derived compound targets, BCL2-associated genes, and cancer-specific transcriptomes. The Venn Diagram Online Tool v2.1.0 revealed significant overlaps across all five cancer models, with the number of intersecting targets varying by cancer type. These shared targets represented the molecular nodes where LCEE phytochemicals could potentially modulate BCL2-dependent survival pathways, thereby sensitizing cancer cells to apoptosis. The identification of common targets across multiple cancer types suggested a broad-spectrum therapeutic potential of LCEE phytochemicals against diverse malignancies sharing BCL2-driven survival mechanisms.

Protein–Protein Interaction (PPI) Network Construction and Hub Gene Identification

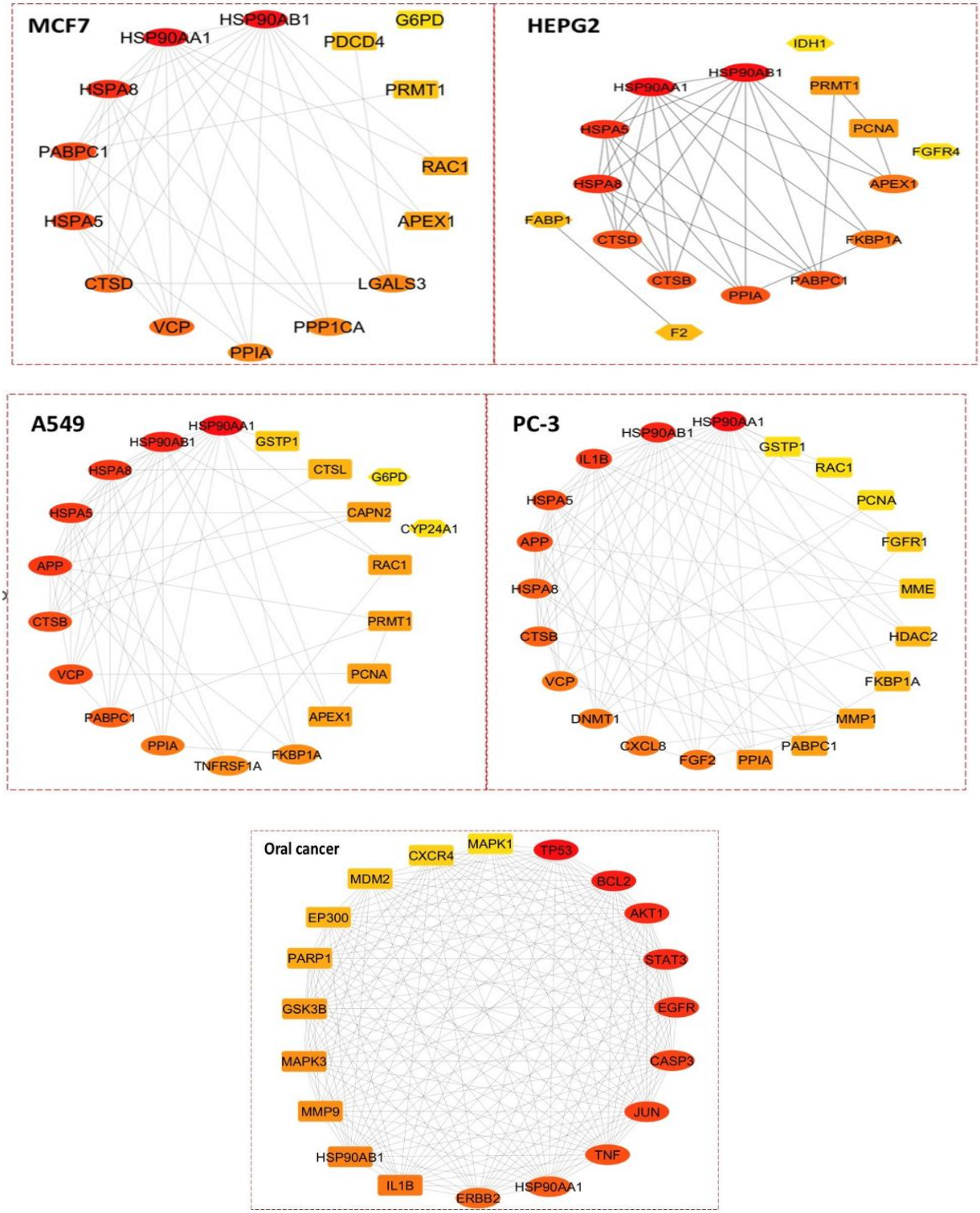

Figure 3: PPI Network of Common Targets with Hub Genes Highlighted in Elliptical Nodes and Red Coloring Indicating Highest Interaction Degree

The targets of every type of cancer were cut into overlapping fragments that were entered in the STRING database (lowest interaction confidence score of 0.4, medium confidence) in order to build comprehensive PPI networks. Topological analysis and visualization were performed in Cytoscape v3.10.4 to import the resulting networks into the software. Statistics on the

networks showed that the complexity of the network of different types of cancers generally differed greatly: prostate cancer had 21 nodes and 75 edges; breast cancer had 15 nodes and 36 edges; liver cancer had 16 nodes and 32 edges; lung cancer had the most connected network with 20 nodes and 181 edges; and oral cancer had 21 nodes and 75 edges. These networks are dependent on the count and the concentration of the common targets in the molecular interaction systems in individual cancer models.

The topological analysis tools of Cytoscape were used in identifying the hub genes (core regulatory nodes with the most connections). In all cancers, the hub genes consistently were those involved in the molecular activity of stabilizing oncogenic client proteins (HSP90AA1, HSP90AB1), lysosomal proteases (CTSD), receptor tyrosine kinase (EGFR), the major executioner caspase (CASP3), the central anti-apoptotic protein (BCL2). These hub genes were pointed out with ellipse shaped nodes in end PPI network diagrams where the node size and color intensity indicates the degree of interaction thus showing importance as possible drug targets in the BCL2 apoptotic axis.

Gene Ontology (GO) and Functional Enrichment Analysis

Biological Process (BP) Enrichment

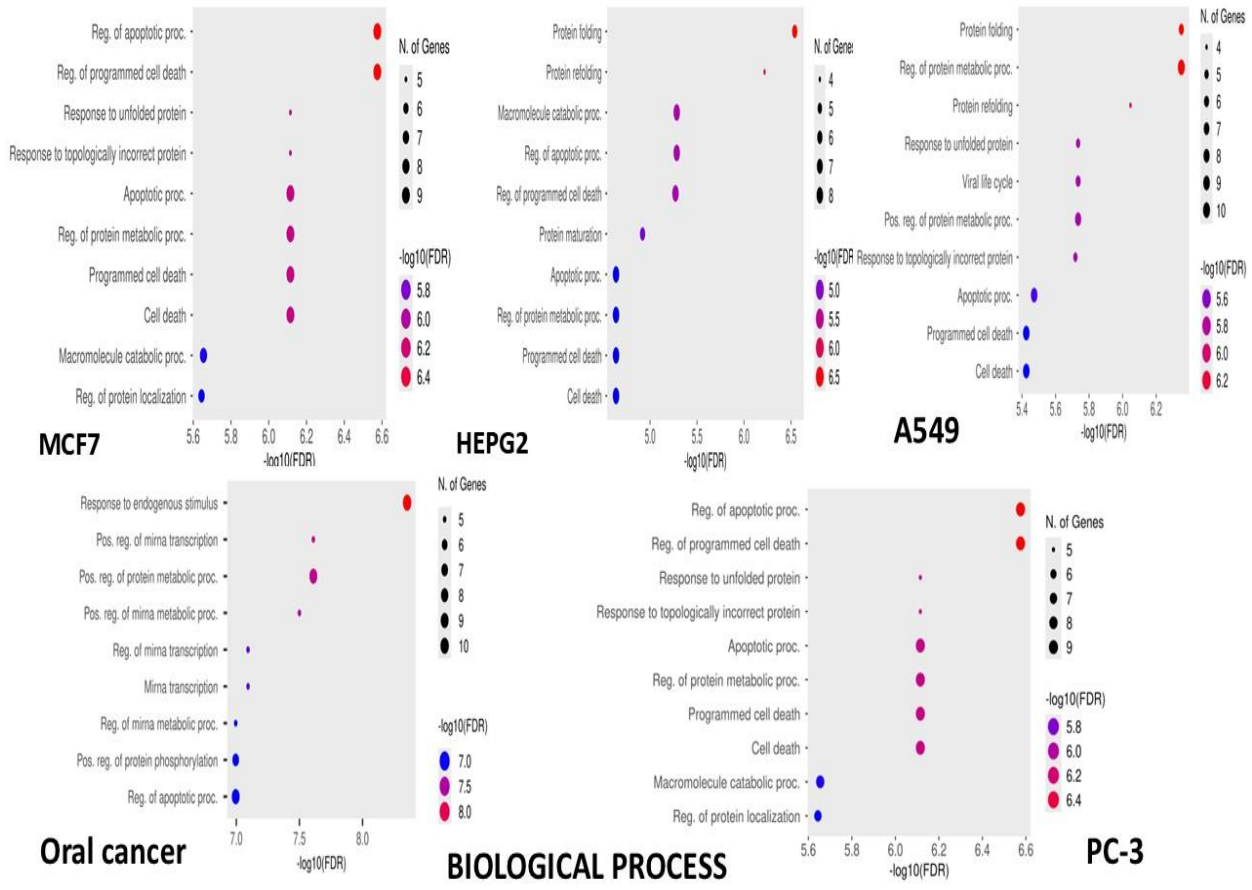

Figure 4: Showing the Biological Processes of the Hubgenes.

GO Biological Process enrichment analysis across all four cancers (prostate, lung, liver and breast) showed coordinated enrichment of pathways of apoptotic regulation, protein quality-control, stress-response signaling, and oncogenic regulation.

Breast Cancer: Breast Cancer: The hub genes of LGALS3, Hsp90AA1, CTSD, Hsp90AB1, Hsp90A8, PPP1CA, Hspa5, PPIA, and VCP supported the most significantly enriched BP terms of regulation of apoptotic process and regulation of programmed cell death (-log10FDR = 6.4).

Lung Cancer: Hub genes displayed enrichment for "protein folding" and "regulation of protein metabolic process" ($-\log_{10}$FDR = 6.2), involving HSPA5, HSP90AA1, HSP90AB1, HSPA8, PPIA, FKBP1A, PABPC1, APP, VCP, and TNFRSF1A. Additional enrichment was detected in protein refolding, unfolded protein response, regulation of proteolysis, and cellular response to heat.

Liver Cancer: Reported proteostasis-mediated BP enrichment, including the most meaningful terms (-log10FDR = 6.5): protein refolding and protein folding, used because of HSPA5, HSPA8, HSP90AA1, HSP90AB1, PPIA and FKBP1A. Further enrichment of macromolecule catabolic process and correlated protein quality-control pathways was also observed.

Oral Cancer: Oral Cancer: This showed a different enrichment trend that was dominated by response to endogenous stimulus (-log10FDR = 8.0) and this involved STAT3, ERBB2, AKT1, CASP3, JUN, TNF, HSP90AA1, TP53, EGFR, and BCL2. Other BP enrichment involved positive regulation of miRNA transcription, regulation of the MAPK cascade, intrinsic apoptotic signaling, cell response to lipid and regulation of inflammatory response.

Prostate Cancer: Prostate cancer paralleled breast cancer through strong enrichment in regulation of apoptotic process and regulation of programmed cell death ($-\log_{10}$FDR = 6.4), supported by LGALS3, HSP90AA1, CTSD, HSP90AB1, HSPA8, PPP1CA, HSPA5, PPIA, and VCP, with additional processes including response to unfolded protein and other stress-related pathways.

As a whole, BP enrichment in all cancers depicted the interaction of apoptosis regulation, proteostasis, stress adaptation, and signal transduction as key pathways that cause LCEE phytochemical activity.

Cellular Component (CC) Enrichment

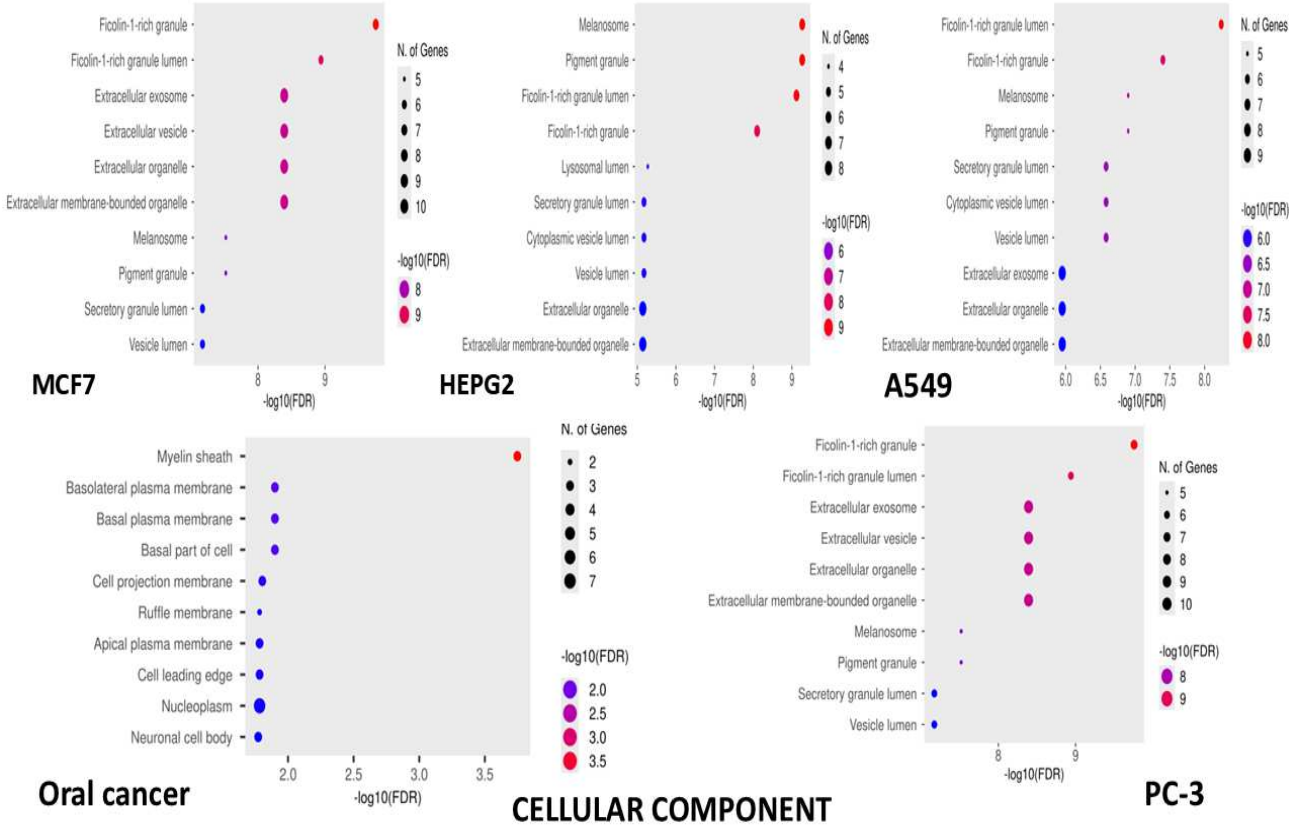

Figure 5: Showing the Cellular Components of the Hubgenes

CC enrichment revealed extensive overlap in vesicle-associated, chaperone-rich, and membrane-associated compartments across the cancer models.

Breast Cancer: "Ficolin-1–rich granule" ($-\log_{10}$FDR = 9.0) and "extracellular exosome" ($-\log_{10}$FDR = 8.0) were the most enriched terms, supported by HSP90AA1, HSP90AB1, HSPA8, CTSD, LGALS3, VCP, PPIA, PABPC1, and PPP1CA. Additional enrichment was noted in cytoplasmic vesicle lumen, lysosomal lumen, and secretory granule.

Lung Cancer: Hub genes were enriched in "melanosome," "pigment granule," and "ficolin-1–rich granule lumen" ($-\log_{10}$FDR = 8.0), contributed by HSPA5, HSP90AA1, HSP90AB1, HSPA8, CTSD, CTSB, and PPIA. Additional terms included lysosomal membrane, endosomal lumen, cytosolic ribonucleoprotein complex, and perinuclear region.

Liver Cancer: Mirrored the lung CC profile with "melanosome," "pigment granule," and "ficolin-1–rich granule lumen" as dominant terms ($-\log_{10}$FDR = 9.0), alongside ficolin-1–rich granule, lysosomal lumen, and secretory vesicle.

Oral Cancer: Primary CC term was "myelin sheath" ($-\log_{10}$FDR = 3.5), driven by HSP90AA1, ERBB2, and BCL2, with additional enrichment in basolateral plasma membrane, focal adhesion sites, receptor complexes, and membrane microdomains.

Prostate Cancer: Prostate cancer aligned with the vesicle-dominant cancers, showing prominent enrichment in ficolin-1–rich granule ($-\log_{10}$FDR = 9.0) through HSP90AA1,

HSP90AB1, HSPA8, CTSD, LGALS3, VCP, and PPIA, and additional localization to ficolin-1–rich granule lumen and related secretory vesicles.

These results collectively underscored the prominence of vesicular, granule-associated, and membrane-related structures in mediating protein homeostasis, signaling, and cellular stress responses across diverse cancer types.

Molecular Function (MF) Enrichment

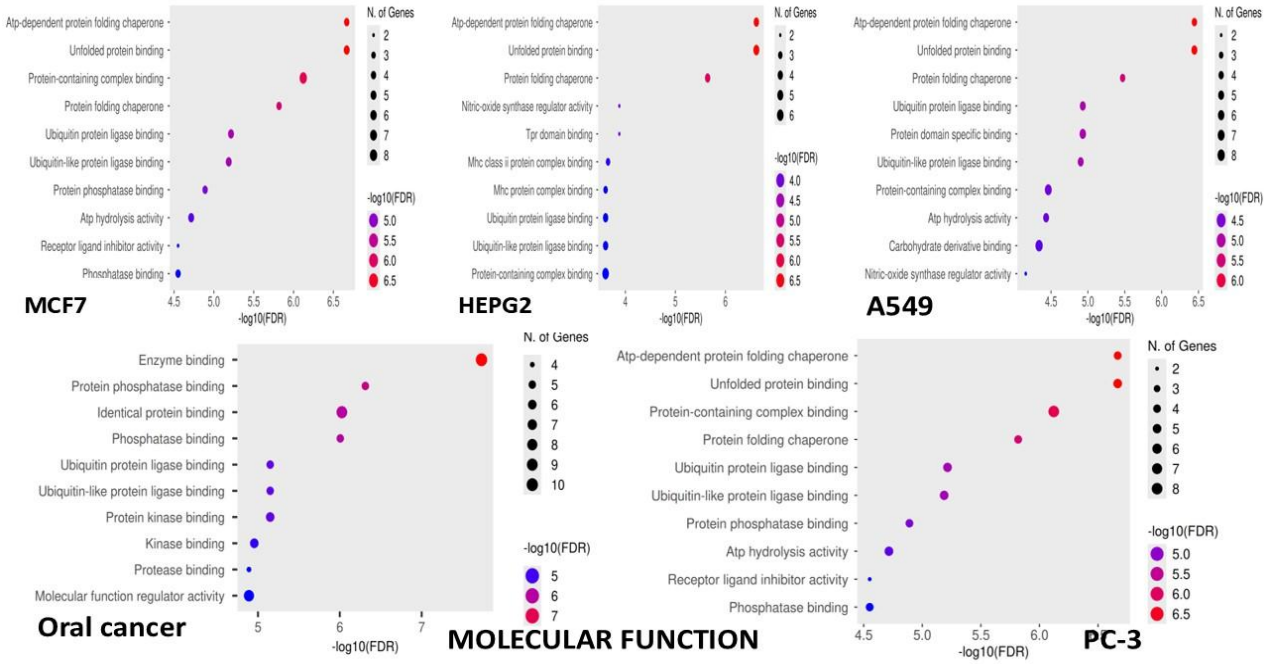

Figure 6: Showing the Molecular Function of the Hubgenes

MF enrichment highlighted chaperone-mediated protein regulation, protein–protein interactions, and enzymatic regulatory activity.

Breast Cancer: Genes were enriched for "ATP-dependent protein-folding chaperone activity" ($-\log_{10}$FDR = 6.5) and unfolded protein binding, with additional MF terms including heat-shock protein binding, protease binding, and ubiquitin-protein ligase regulator activity.

Lung Cancer: Hub genes displayed "ATP-dependent protein-folding chaperone activity" and "unfolded-protein binding" ($-\log_{10}$FDR = 6.0), with additional enrichment in peptidyl-prolyl cis-trans isomerase activity, protein-disulfide reductase activity, and protein-binding functions.

Liver Cancer: Shared similar MF enrichment showing "ATP-dependent protein-folding chaperone activity" and "unfolded-protein binding" ($-\log_{10}$FDR = 6.5), alongside nitric-oxide synthase regulator activity and other proteostasis-related functions.

Oral Cancer: Dominant MF term was "enzyme binding" ($-\log_{10}$FDR = 7.0), involving TP53, ERBB2, BCL2, HSP90AA1, AKT1, EGFR, CASP3, STAT3, TNF, and JUN, with additional enriched functions in protein phosphatase binding, kinase regulator activity, transcription factor binding, and ubiquitin-protein ligase binding.

Prostate Cancer: Prostate cancer presented a consistent proteostasis signature, exhibiting ATP-dependent protein-folding chaperone activity and unfolded-protein binding ($-\log_{10}$FDR = 6.5) driven by HSPA5, HSP90AA1, HSP90AB1, HSPA8, and PPIA, and further enrichment in protein-containing complex binding.

Together, these MF enrichments revealed a coordinated regulatory network governing protein folding, enzymatic modulation, and signal transduction across all cancer types.

KEGG Pathway Enrichment Analysis

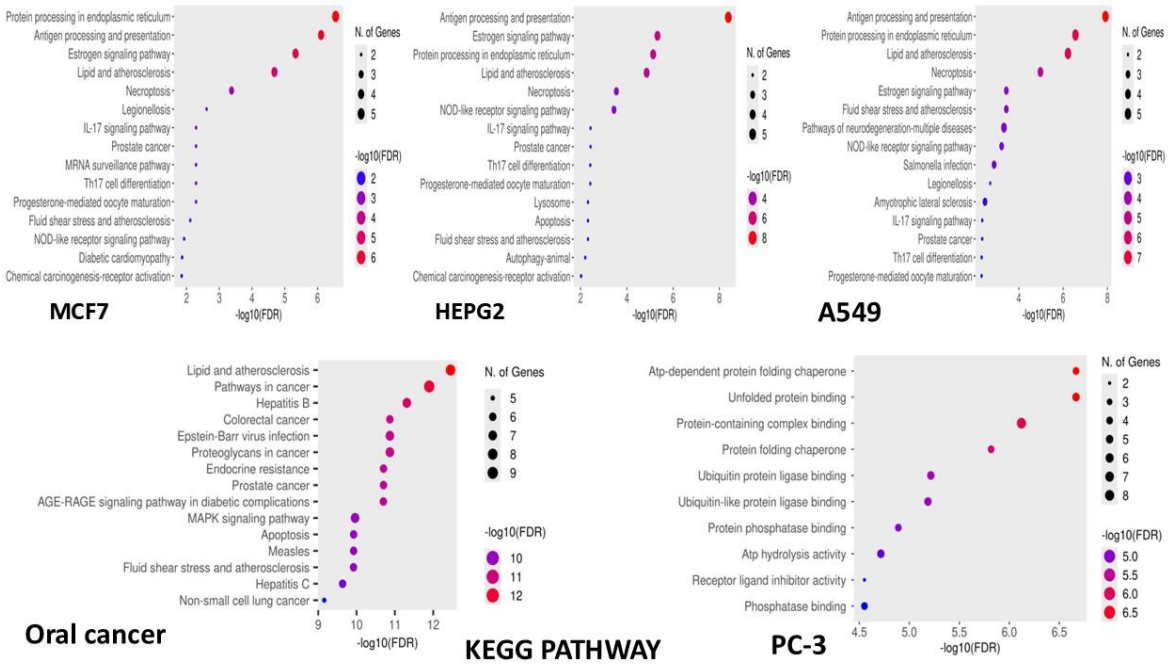

Figure 7: Showing the KEGG Pathway of the Hubgenes

KEGG pathway enrichment revealed common and cancer-specific signaling networks underlying BCL2-mediated survival between the five cancer models.

Breast Cancer: The top pathway (- log10FDR = 6.0) was the endoplasmic reticulum protein processing, and secondary enrichments were in apoptosis, estrogen signaling, proteasome and lysosome pathways.

Lung Cancer: Was dominated by the actinogen processing and presentation (-log10FDR = 7.0), estrogen signaling, NOD-like receptor signaling, endocytosis, and protein export.

Liver Cancer: Displayed -log10FDR = 8.0 antigen processing and presentation as the most significantly enriched pathway, and estrogen signaling, endocytosis, and lysosomal pathways as supplementary enrichment.

Oral Cancer: The highest enrichment levels, both of which are -log10FDR = 12, were in hepatitis B, MAPK signaling, TNF signaling, and PI3K-Akt signaling.

Prostate Cancer: Prostate cancer demonstrated strong enrichment in protein processing in the endoplasmic reticulum and antigen processing and presentation ($-\log_{10}$FDR = 6.0), driven by

HSPA5, HSPA8, HSP90AA1, HSP90AB1, and VCP, with additional involvement in estrogen signaling and other proteostasis-associated pathways.

In general, KEGG analysis identified the commonality of proteostasis, immune regulation, and canonical oncogenic signaling in the four types of cancer.

Molecular Docking and Validation

Table 1: Identification of Compounds

S/N	Pubchem CID	Compound name	ID
1	2117	(+-)-Alpha-Tocopherol Acetate acid Ester	S1
2	6076	Adenosine-3',5'-Cyclicmonophosphate	S2
3	16219760	Beta-Nicotinamide Adenine Dinucleotide Hydrate	S3
4	5892	Beta-Nicotinamide Adenine Dinucleotide Oxidized Form	S4
5	5281227	Canthaxanthin	S5
6	165559	Delphinidin-3-O-Beta-Glucopyranoside	S6
7	3442	Fusaric_Acid	S7
8	135398570	Guanosine-3',5'-Cyclic_Monophosphate	S8
9	88513	Leucylleucyltyrosine	S9
10	6057	L-Tyrosine	S10
11	6441269	Marein	S11
12	23900088	Myricetin-3-Xyloside	S12
13	135445758	Nicotinamide hypoxanthine dinucleotide sodium salt (2)	S13
14	5283565	N-Stearoyl-D-Erythro-Sphingosine	S14
15	2723800	Safranine	S15
16	192751	UDP-Beta-L-Rhamnose	S16
17	5280899	Zeaxanthin	S17

Docking Protocol Validation

To verify the reliability of the molecular docking workflow, the validation was done with HSP90AB1 (PDB: 6N8Y), which was one of the top-scoring hub proteins identified in the network analysis. It was extracted and redocked into the protein with the same Glide XP parameters with the original co-crystallized ligand. The RMSD of crystallographic poses between the redocked and original crystallographic was 0.5472 Å, which validated the validity and the reproducibility of the docking protocol.

Lead Compound Identification and Docking Scores

Table 2. Docking Result for Druggable Target and Resolution

Ligand (ID)	HSP90AB1 6N8Y	CTSD 6QBG	LGALS3 7CXA	HSP90AA1 1UYM	CASP3 3H0E	BCL2 8HTR	EGFR 3W2S
S1	-6.244	-3.819	-1.448	-3.195	-2.589	-5.539	-1.819
S2	-6.86	-6.626	-3.534	-6.776	-5.389	-5.148	-9.82

S3	-14.544	-8.446	-7.935	-12.907	-13.28	-9.418	-10.707
S4	-15.88	-9.708	-9.208	-5.216	-10.418	-9.037	-10.254
S5	—	—	—	—	—	-2.751	—
S6	-11.642	-10.637	-6.528	-13.01	-9.944	-5.666	-11.022
S7	-7.488	-5.691	-2.829	-7.804	-5.002	-4.508	-4.565
S8	-7.604	-5.991	-3.081	-7.393	-5.714	-5.345	-7.927
S9	-7.274	-6.677	-2.889	-9.854	-7.911	-6.233	-7.488
S10	-7.509	-5.839	-2.864	-7.578	-4.448	-4.008	-6.291
S11	-12.64	-11.898	-5.545	-11.973	-9.733	-7.664	-10.661
S12	-11.77	-9.322	-6.994	-12.841	-9.324	-6.591	-10.796
S13	-12.934	-8.984	-5.603	-11.739	-9.473	-7.13	-13.205
S14	—	—	0.326	—	-4.373	-4.398	-3.704
S15	-4.303	-5.251	-2.362	-4.62	-4.481	-4.545	-5.604
S16	-12.619	-11.18	-7.471	-12.41	-9.672	-7.338	-9.572
S17	—	—	—	—	—	—	—
RESOLUTION	**1.55**	**1.80**	**1.97**	**2.45**	**2.00**	**1.60**	**1.90**

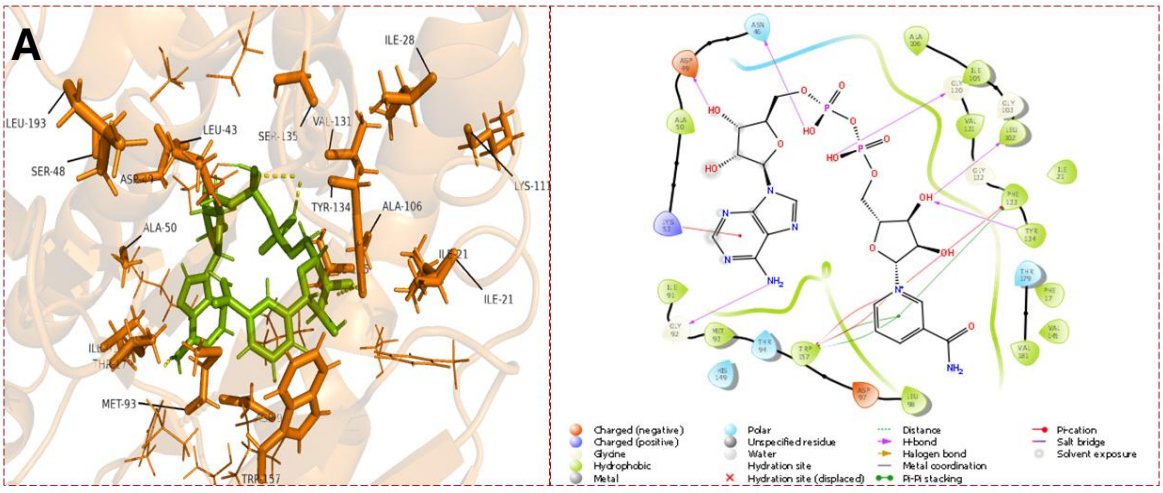

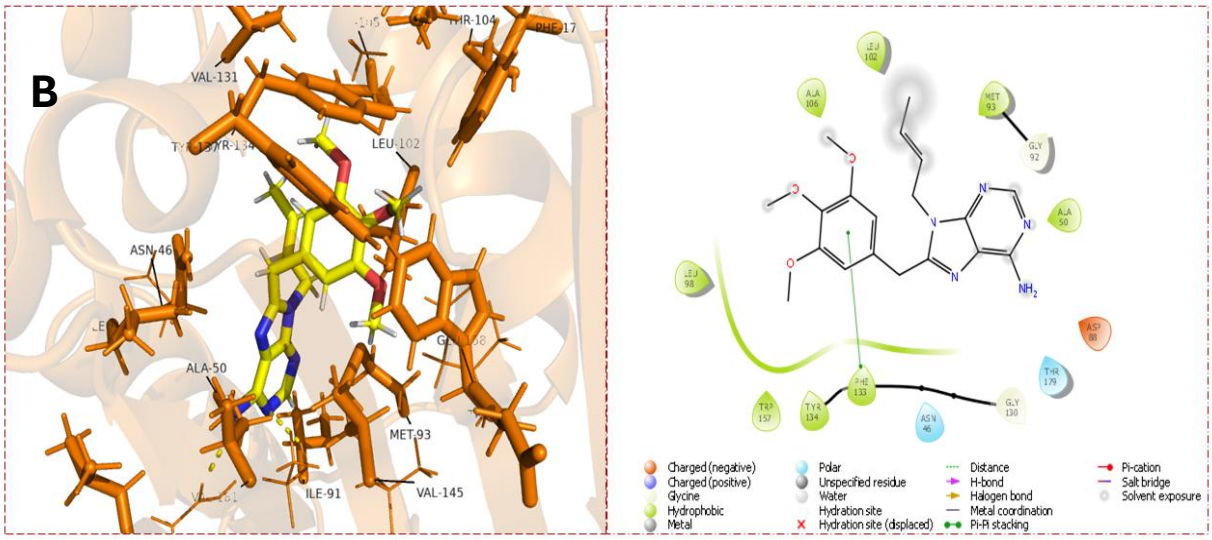

Figure 8: 3D and 2D visualization of best complex- 6N8Y with compound S4 (A) and Native Ligand (B)

Figure 9. Docking Validation

Based on network pharmacology predictions, 24 unique hub genes were identified across the five cancer models. From these, seven proteins with well-defined binding pockets and confirmed druggability were prioritized for molecular docking: HSP90AB1 (6N8Y), HSP90AA1 (1UYM), CTSD (6QBG), LGALS3 (7CXA), CASP3 (3H0E), BCL2 (8HTR), and EGFR (3W2S). All 18 LCEE phytochemicals were docked into these target proteins using Glide in Extra Precision (XP) mode.

HSP90AB1 (6N8Y): The strongest binding affinities were obtained for S4 (−15.88 kcal/mol) and S3 (−14.54 kcal/mol), followed by S13 (−12.93 kcal/mol) and S11 (−12.64 kcal/mol).

HSP90AA1 (1UYM): S6 (−13.01 kcal/mol) and S3 (−12.91 kcal/mol) showed the most favorable interactions.

CTSD (6QBG): S11 (−11.90 kcal/mol) emerged as the top-scoring ligand, with favorable interactions supporting its role as a lead compound targeting lysosomal proteases implicated in liver and breast cancers.

LGALS3 (7CXA): S4 (−9.21 kcal/mol) showed the strongest binding interaction, relevant to breast cancer progression where LGALS3 plays a critical regulatory role.

EGFR (3W2S): S13 displayed the most favorable binding (−13.21 kcal/mol), alongside high-affinity interactions for S3 (−10.70 kcal/mol) and S6 (−11.02 kcal/mol), relevant to prostate and oral cancer models driven by receptor tyrosine kinase signaling.

CASP3 (3H0E): S3 (−13.28 kcal/mol) produced the most favorable docking score, indicating potential enhancement of apoptotic execution.

BCL2 (8HTR): S3 (−9.42 kcal/mol) and S4 (−9.04 kcal/mol) displayed moderate binding affinities within the canonical hydrophobic BH3-binding groove.

Based on these multi-target docking profiles, S4, S3, S6, S11, and S13 were identified as principal lead compounds with broad therapeutic potential across the five cancer models.

Binding Free Energy Estimation (MM-GBSA)

To provide additional thermodynamic validation of protein–ligand interactions, MM-GBSA analysis was performed on the top-ranked complexes identified in docking. The binding free energy (ΔG_bind) was calculated using the equation:

$$\Delta G_{\text{bind}} = G_{\text{complex}} - \left(G_{\text{protein}} + G_{\text{ligand}}\right)$$

where G_complex is the free energy of the receptor–ligand complex, G_protein is the free energy of the protein in the absence of the ligand, and G_ligand is the free energy of the free ligand.

MM-GBSA results provided strong thermodynamic support for the stability of lead compounds:

- **S4 (HSP90AB1):** ΔG_bind = −87.21 kcal/mol, indicating highly stable complex formation
- **S3 (EGFR):** ΔG_bind = −84.14 kcal/mol, reflecting excellent binding stability
- **S6 (EGFR):** ΔG_bind = −64.14 kcal/mol, confirming favorable thermodynamics
- **S11 (CTSD):** ΔG_bind = −61.40 kcal/mol, supporting stable lysosomal protease targeting
- **S13 (EGFR):** ΔG_bind = −46.46 kcal/mol, indicating favorable receptor engagement

These energetically favorable binding profiles reinforce that the identified interactions are likely to persist under physiological conditions.

In Silico ADMET Profiling

ADMETLab 3.0 was used to evaluate all 18 LCEE phytochemicals in silico and the five lead compounds (S3, S4, S6, S11, S13) were analyzed in detail.

Absorption and Distribution Parameters

Table 3: Absorption and Distribution Analysis of Compound

ABSOPTION AND DISTRIBUTION							
S/N	**PubChem ID**	**Pgp Inhibitor**	**Pgp Substrate**	**HIA**	**Caco-2**	**PPB**	**VDss**
1	2117	Non-inhibitor	Non-substrate	Low	Optimal	High	Optimal
2	6076	Non-inhibitor	Non-substrate	Low	Low	Optimal	Low
3	16219760	Non-inhibitor	Non-substrate	Low	Suboptimal	Optimal	Low
4	5892	Non-inhibitor	Non-substrate	Low	Suboptimal	Optimal	Suboptimal
5	5281227	Non-inhibitor	Non-substrate	High	Optimal	High	Optimal
6	165559	Non-inhibitor	Non-substrate	High	Low	Optimal	Low
7	3442	Non-inhibitor	Non-substrate	Low	Optimal	High	Low
8	135398570	Non-inhibitor	Non-substrate	High	Low	Optimal	Low
9	88513	Non-inhibitor	Non-substrate	Low	Low	Optimal	Low
10	6057	Non-inhibitor	Substrate	High	Low	Optimal	Optimal
11	6441269	Non-inhibitor	Non-substrate	High	Low	High	Optimal
12	23900088	High (Inhibitor)	High (Substrate)	High	Optimal	High	Optimal
13	135445758	Non-inhibitor [1]	Non-substrate [2]	Low	Low	Optimal	Low
14	5283565	Non-inhibitor	Non-substrate	Low	Low	High	Optimal
15	2723800	Non-inhibitor	Non-substrate	High	Optimal	High	Optimal
16	192751	High (Inhibitor)	High (Substrate)	Low	Low	Optimal	Low
17	5280899	Non-inhibitor	Non-substrate	High	Optimal	High	Optimal

The five lead compounds were predicted to be non-inhibitors and non-substrates of P-glycoprotein indicating minimal efflux transporter-mediated clearance. S6 and S11 were found to have high predicted human intestinal absorption (HIA) whereas S3, S4, and S13 were found to have low absorption, which may inhibit oral bioavailability. The permeability of the Caco-2 cell was also not constant and S4 and S6 exhibited optimal permeability as compared to the others which had suboptimal values. The predictions were that plasma protein binding should be optimal in the case of S3, S4 and S13 and high in S11. Volume of distribution (VDss) ranged from low to optimal across the leads. Blood–brain barrier (BBB) penetration was predicted to be low for all five compounds, which is favorable for minimizing potential neurotoxicity while maintaining periphery-directed anticancer activity.

Metabolism and Excretion Profiles

Table 4: Metabolism and Excretion Analysis of Compound

METABOLISM AND EXCRETION							
S/N	**PubChem ID**	**CYP3A4 Inhibitor**	**CYP3A4 Substrate**	**CYP2C9 Inhibitor**	**HLM**	**CLplasma**	**T1/2**
1	2117	High	High	High	Low (Unstable)	Optimal (Moderate)	Low (Ultra-short)
2	6076	Non-inhibitor	Non-substrate	Non-inhibitor	High	Low	short
3	16219760	Non-inhibitor	Non-substrate	Non-inhibitor	High	Low	short
4	5892	Non-inhibitor	Non-substrate	Non-inhibitor	High	Low	short
5	5281227	High	High	Non-inhibitor	Low (Unstable)	High	Low (Ultra-short)
6	165559	Non-inhibitor	Non-substrate	Non-inhibitor	High (stable+)	Low	Intermediate short
7	3442	Inhibitor	Non-substrate	Non-inhibitor	Low (Unstable)	Low	long
8	135398570	Non-inhibitor	Non-substrate	Non-inhibitor	High	Low	Intermediate short

9	88513	Non-inhibitor	Non-substrate	Non-inhibitor	High	Low	short
10	6057	Non-inhibitor	Non-substrate	Non-inhibitor	High (Stable)	High	Short
11	6441269	Non-inhibitor	Non-substrate	Non-inhibitor	High (Stable)	Low	High (Long)
12	23900088	Non-inhibitor	Non-substrate	Non-inhibitor	High (Stable)	Low	Intermediate
13	135445758	Non-inhibitor	Non-substrate	Non-inhibitor	High (Stable)	Low	Short
14	5283565	Non-inhibitor	Non-substrate	Non-inhibitor	High (Stable)	Low	Short
15	2723800	Non-inhibitor	Non-substrate	Non-inhibitor	High (Stable)	Low	High (Long)
16	192751	Non-inhibitor	Non-substrate	Non-inhibitor	High (Stable)	Low	High (Long)
17	5280899	Non-inhibitor	Non-substrate	Non-inhibitor	High (Stable)	Low	High (Long)

All five lead compounds were predicted to be non-inhibitors and non-substrates of the major cytochrome P450 enzymes (CYP3A4 and CYP2C9), indicating low potential for CYP-mediated drug–drug interactions. Human liver microsomal (HLM) stability was predicted to be high for S3, S4, S6, and S13, with S11 also displaying acceptable metabolic stability. Plasma clearance was uniformly predicted to be low across all leads, suggesting extended circulation half-lives favorable for sustained systemic exposure. Half-life predictions indicated short half-lives for S3, S4, and S13 (likely due to rapid conjugation or renal clearance), an intermediate-short half-life for S6, and a notably long half-life for S11, which may be favorable for less frequent dosing.

Toxicity Predictions

Table 5: Toxicity Prediction of Compound

TOXICITY						
S/N	**PubChem ID**	**hERG Inhibition**	**Ames Mutagenicity**	**Carcinogenicity**	**Hepatotoxicity (Human)**	**Skin Sensitization**
1	2117	High	Low	Low	High	High
2	6076	Low	High	Moderate	Moderate	High
3	16219760	Low	Low	High	Low	High
4	5892	Low	High	Moderate	Low	High
5	5281227	High	Low	High	High	High
6	165559	Low	High	Low	Moderate	High
7	3442	Low	Low(negative)	Low	Low	Low
8	135398570	Low	High	Low	Moderate	High
9	88513	Low	Low	Low	High	High
10	6057	Low	High	Low	High	High
11	6441269	Low	Low	Low	High	High
12	23900088	Low	Low	Low	Low	High
13	135445758	Low	Low	Low	Low	High
14	5283565	High	Low	Low	High	High
15	2723800	Low	Low	Low	High	High
16	192751	Low	Low	Low	Low	High
17	5280899	Low	Low	Low	Low	Low

hERG potassium channel inhibition risk (a cardiotoxicity indicator) was predicted to be low for S3, S4, S6, S11, and S13, suggesting minimal cardiac liability. Ames's mutagenicity was predicted negative for S3, S11, and S13, but positive for S4 and S6, warranting further safety assessment in follow-up studies. S3, S4, and S6 had positive, moderately positive and negative carcinogenicity respectively. S3 and S13 were predicted to be in the low category, S6 in the moderate category and S11 in the high category with regard to hepatotoxicity and thus they need monitoring. Sensitization of the skin was also predicted to be high in S3, S4, S6, and S11 and low in S13, but this parameter is mainly important with topical but not systemic use.

The ADMET profiling combined with supported the drug-likeness of the lead compounds and their possible utility as scaffolds to develop anticancer drugs, acceptable pharmacokinetic properties and appropriate toxicity risks.

Discussion

Drunkenness of apoptosis is one of the most basic survival mechanisms of cancer cells, and anti-apoptotic protein BCL2 plays a central regulatory role in this mechanism [34-36]. BCL2 also inhibits the mitochondrial outer membrane permeabilization (MOMP) by binding pro-apoptotic effectors, including BAX and BAK, inhibiting cytochrome-c release and the subsequent executioner caspase activation [34,37]. Lasting BCL2 expression has also been reported in a variety of solid tumors such as lung, liver, breast, prostate, and oral cancers, where it helps in tumor progression, therapeutic resistance and poor patient outcomes [35,36,38]. Therefore, direct inhibition or disruption of the BCL2 signaling axis regulatory network is likely to be highly promising as an anticancer strategy[39,40].

This combined analysis used LC-MS phytochemical profiling, network pharmacology, molecular docking, MM-GBSA binding energy, and in silico ADMET modeling to reveal the mechanistic nature of how phytochemical constituents of Lantana camara identified by systematic LC-MS analysis can mediate BCL2-associated survival networks in five different cancer types [41-43].The concordance between experimental cytotoxicity data (IC_{50} values of 76.62–132.4 μg/mL), network pharmacology predictions (753 compound targets overlapping BCL2 pathways), docking affinities (−15.88 to −9.04 kcal/mol), and MM-GBSA binding free energies (−87.21 to −46.46 kcal/mol) provides a biologically coherent and mechanistically anchored rationale for the multi-cancer relevance of the identified lead compounds [42,44].

The network pharmacology analysis established that the molecular targets of LCEE phytochemicals converge extensively with BCL2-associated genes and cancer-specific transcriptional signatures [41,45]. Protein–protein interaction analysis demonstrated that intersecting target sets organize into tightly connected hubs dominated by stress-response proteins (HSP90 family), lysosomal proteases (CTSD), receptor tyrosine kinases (EGFR, ERBB2), inflammatory mediators (TNF, JUN, STAT3), kinases (AKT1), and the apoptotic machinery (CASP3, BCL2) [45-47]. Gene Ontology enrichment revealed that across all five cancers, dominant biological processes revolve around apoptosis regulation, protein folding and unfolded protein response, stress adaptation, proteolysis, and oncogenic signaling. These shared biological programs reinforce the centrality of proteostasis and apoptotic control as cross-cancer vulnerabilities within the BCL2 regulatory axis [42,48].

The docking and MM-GBSA analyses revealed the molecular-level mechanisms by which LCEE phytochemicals engage the BCL2 network. Compounds S3 and S4 exhibited stable binding within the canonical hydrophobic groove of BCL2 that normally accommodates pro-apoptotic BH3-only proteins [6,49]. While the absolute binding energies of S3 and S4 for BCL2 were moderate relative to classical BH3 mimetics (such as venetoclax), their functional relevance is amplified by the fact that these compounds simultaneously disrupt upstream survival signaling and protein-stabilization machinery identified in the GO and KEGG analyses [39,40,49].

A dominant indirect mechanism is mediated through the molecular chaperone HSP90, which emerged as one of the most consistently enriched hub proteins across breast, lung, liver, and prostate cancers. S3 and S4 displayed particularly strong binding affinities to HSP90AB1, while S6 showed preferential engagement with HSP90AA1 [50,51]. HSP90 functions as a central stabilizing platform for multiple oncogenic client proteins, including AKT1, STAT3, EGFR, and ERBB2, all of which are transcriptional or post-translational regulators of BCL2 expression [51,52]. Inhibition of HSP90 produces a cascading destabilization effect in which upstream survival kinases and transcription factors undergo misfolding and proteasomal degradation, leading to secondary suppression of BCL2-driven anti-apoptotic signaling. This chaperone-dependence is fully consistent with the strong enrichment of protein folding, unfolded protein response, ER protein processing, and proteasome-related KEGG pathways observed across the cancers analyzed [50,53].

Lysosomal control of apoptotic sensitivity represents a second indirect regulatory axis supported by the docking data. S11 exhibited the strongest and most stable binding to CTSD, a lysosomal aspartic protease consistently enriched in vesicle- and granule-associated cellular components across multiple cancers [54,55]. Cathepsin D is a recognized mediator of lysosomal–mitochondrial crosstalk during stress-induced apoptosis. Its dysregulation can promote lysosomal membrane permeabilization, resulting in cytosolic release of cathepsins that cleave BID and promote MOMP. Through this mechanism, modulation of CTSD by S11 provides an additional BCL2-independent route for lowering the apoptotic threshold and reinforcing mitochondrial commitment to cell death, further weakening BCL2-mediated resistance [54-56].

In oral cancer, where GO and KEGG analyses demonstrated dominant enrichment of receptor-mediated signaling, inflammatory response, MAPK cascade, PI3K–Akt signaling, and canonical oncogenic pathways, the docking results reveal a complementary mode of action [57]. S13 had a high affinity to EGFR, whereas S3 interacted at EGFR and AKT- associated nodes. Such interactions directly hit on key upstream drivers which sustain persistent activation of STAT3 and AKT [58]. Since STAT3 and AKT are both established transcriptional enhancers and post-translational stabilizers of BCL2, inhibition of these signaling pathways presents a direct regulatory pathway of silencing BCL2 protein and activity of signaling-dominant tumors [59].

During the final apoptotic stage, S3 demonstrated the highest binding affinity to CASP3 which is the main executioner caspase that causes the cell to be broken permanently. The mechanistic

role of this interaction is that it implies that, in addition to S3 undermining anti- apoptotic protective mechanisms at the mitochondrial level by interfering with BCL2 and suppressing upstream signaling, it also promotes the efficiency of apoptotic execution [60,61]. This twofold effect, of a concerted interference with both the initiation and execution stages of intrinsic apoptosis, is in line with convergence of CASP3, TP53, TNF, JUN, EGFR, and BCL2 in the oral cancer hub-gene network [52,58].

The in silico ADMET profiling revealed that the most successful compounds have good physicochemical and pharmacokinetic properties that can be used in the systemic exposure, intestinal absorption, and can be treated by toxicity. They are our drug-like scaffold of choice because of the lack of significant predicted cardiotoxicity and hepatotoxicity liabilities, as well as acceptable metabolic stability [62,63]. Significantly, these are pharmacokinetic properties that support the multi-target molecular profile of docking and MM-GBSA in the context that the compounds may be plausibly located in intracellular portals like the cytosol, lysosome, and mitochondria where BCL2, HSP90, CTSD, and CASP3 are located [62].

Put differently, the combined outcome of this combined analysis shows that the effects of *Lantana camara* phytochemicals are neither based on single-target action nor on a multi-level disruption but rather on a multi-level, coordinated action in the BCL2 survival network. This involves direct mitochondrial antagonism by occupating BCL2 grooves, disrupting chaperone-mediated stabilization by inhibiting HSP90, amplifying mitochondrial stress by this means of CTSD, inhibiting upstream receptor-kinase signalling through EGFR and AKT interactions, and potentiating executioner caspase activation by binding CASP3. The agreement between network pharmacology, GO/KEGG enrichment, docking, MM-GBSA and ADMET analysis results offers a biologically consistent and mechanistically based explanation of the multi-cancer applicability of the identified lead compounds. These results make LCEE phytochemicals attractive as useful targets to study with activity-based fractionation, structure-activity relationships, and in vivo follow-up to the creation of new anticancer therapeutics in BCL2-survival pathways.

Conclusion

The current article combines in silico systems-level and in vitro cytotoxicity studies to outline the anticancer effect of Lantana camara ethanolic leaf extract (LCEE). LCEE was found to have dose-dependent growth inhibitory effects on A549, MCF-7, PC-3, KB-3-1, and HepG2 cells with IC50 of 76.62 -132.4 ug/mL and maximum inhibition of 65.5-83.7% in vitro indicating a wide, intermediate cytotoxic range across lung, breast, prostate, oral, and liver cancers. LC-MS profiling revealed 18 constituents, including beta-nicotinamide adenine dinucleotide hydrate (S3), its oxidized form (S4), delphinidin-3-O-b-glucopyranoside (S6), marein (S11), and nicotinamide hypoxanthine dinucleotide sodium salt (S13), which became the key candidates to be used in the context of mechanistic exploration. Network pharmacology demonstrated that BCL2-associated genes and cancer transcriptomes have a high density of targets of these phytochemicals, and these form hubs involving apoptosis regulation, proteostasis (HSP90AA1/HSP90AB1), lysosomal processes (CTSD), receptor tyrosine kinase signaling (EGFR/ERBB2), and executioner caspase activity (CASP3). The molecular docking

and MM-GBSA studies also revealed that S3, S4, S6, S11 and S13 can stably interact with several nodes of the BCL2-centered network, including HSP90 isoforms, CTSD, EGFR, CASP3, and BCL2 itself, with docking scores as low as -15.88 kcal/mol and binding free energies as low as -87.21 kcal/mol indicating the best complex. In silico ADMET profiling indicated that these leads had acceptable drug-likeness, metabolic stability was generally favorable, and predicted cardiotoxicity (hERG inhibition) and metabolism-controllable hepatotoxicity and mutagenicity flags, which should not be used as an exclusion criterion at this point but should be subject to structured follow-up testing. An integrated set of results on convergence of in vitro cytotoxicity, multi-target docking, network enrichment and ADMET predictions suggest that the anticancer effects of LCEE result from a concerted action of BCL2-controlled apoptotic and stress-adaptation pathways instead of a single high-potency cytotoxin. These results present L. camara phytochemicals, especially S3, S4, S6, S11, and S13, as promising scaffolds in terms of activity-guided fractionation, SAR optimization, and in vivo validation in the development of polypharmacological BCL2-HSP90-EGFR axis modulators. The future research should focus on single constituent isolation, verification of target interaction in cell-based assays, assessment of efficacy and safety in appropriate animal models to convert these combined in vitro and in silico findings into preclinical anticancer leads.

Acknowledgments

The authors thank the National Centre for Cell Sciences (NCCS), Pune, for providing authenticated cancer cell lines.

Funding

No funding received.

References

1. World Health Organization. (2024). Global cancer burden growing, amidst mounting need for services. International Agency for Research on Cancer. https://www.who.int/news/item/01-02-2024-global-cancer-burden-growing--amidst-mounting-need-for-services
2. Bray, F., Laversanne, M., Sung, H., Ferlay, J., Siegel, R. L., & Soerjomataram, I. (2024). Global cancer statistics 2022: GLOBOCAN estimates of incidence and mortality worldwide for 36 cancers in 185 countries. *CA: A Cancer Journal for Clinicians*, 74(3), 229–263. https://doi.org/10.3322/caac.21834
3. American Cancer Society. (2025). Cancer Facts & Figures 2025. American Cancer Society.
4. Sung, H., Ferlay, J., Siegel, R. L., Laversanne, M., Soerjomataram, I., Jemal, A., & Bray, F. (2021). Global cancer statistics 2020: GLOBOCAN estimates of incidence and mortality worldwide for 36 cancers in 185 countries. *CA: A Cancer Journal for Clinicians*, 71(3), 209–249. https://doi.org/10.3322/caac.21660
5. Carvalho, C., Santos, R. X., Cardoso, S., Correia, S., Oliveira, P. J., Santos, M. S., & Moreira, P. I. (2009). Oxidative stress in anthracycline cardiotoxicity. *Redox Biology*, 1(1), 467–472. https://doi.org/10.1016/j.redox.2009.11.004

6. Gottesman, M. M., Fojo, T., & Bates, S. E. (2002). Multidrug resistance in cancer: role of ATP-dependent transporters. *Nature Reviews Cancer*, 2(1), 48–58. https://doi.org/10.1038/nrc706
7. Doroshow, D. B., Bhalla, S., Beasley, M. B., Chung, J. H., Drive, S. T., Merghoub, T., ... & Stein, J. L. (2019). PD-L1 as a biomarker of response to immune-checkpoint inhibitors. *Nature Reviews Clinical Oncology*, 16(6), 345–362. https://doi.org/10.1038/s41571-019-0173-9
8. Prasad, V., & Mailankody, S. (2017). Cancer drugs approved based on biomarker trials: are they effective in the real world? *JAMA*, 318(3), 241–242. https://doi.org/10.1001/jama.2017.8329
9. Newman, D. J., & Cragg, G. M. (2020). Natural products as sources of new drugs over the nearly four decades from 01/1981 to 09/2019. *Journal of Natural Products*, 83(3), 770–803. https://doi.org/10.1021/acs.jnatprod.9b01285
10. Cragg, G. M., & Newman, D. J. (2013). Natural products: A continuing source of novel drug leads. *Biochimica et Biophysica Acta (BBA) - General Subjects*, 1830(6), 3670–3695. https://doi.org/10.1016/j.bbagen.2013.02.008
11. Desai, A. G., Qazi, G. N., Ganju, R. K., El-Tamer, M., Singh, J., Saxena, A. K., ... & Bhat, H. K. (2008). Medicinal plants and cancer chemoprevention. *Current Drug Metabolism*, 9(7), 581–591. https://doi.org/10.2174/138920008785821657
12. Efferth, T., & Koch, E. (2011). Complex interactions between phytochemicals. The multi-target therapeutic concept of phytotherapy. *Current Drug Targets*, 12(1), 122–132. https://doi.org/10.2174/138945011793591626
13. Zhang, W., Huai, Y., Miao, Z., Yin, A., & Zhang, S. (2020). Systems pharmacology for investigation of the mechanisms of action of traditional Chinese medicine in drug discovery. *Frontiers in Pharmacology*, 11, 1147. https://doi.org/10.3389/fphar.2020.01147
14. Liang, H., Shao, H., Sun, X., Zhang, Y., Dong, C., & Pang, W. (2021). Application of network pharmacology in herbal medicine research: An overview. *Current Bioinformatics*, 16(1), 21–33. https://doi.org/10.2174/1574893615999201026152420
15. Sharma, B., Viswanath, G., Salunke, P., & Roy, P. (2012). Effects of flavonoid-rich extract of Alpinia calcarata Rosc. on melanin synthesis and antioxidant pathways in B16 melanoma cells. *Journal of Agricultural and Food Chemistry*, 60(26), 6527–6535. https://doi.org/10.1021/jf301322t
16. Chukwuma, C. A., Souto, E. B., & Zielinska, A. (2021). *Lantana camara* L. as a source of pharmacologically active phytochemicals: A review. *Molecules*, 26(16), 4880. https://doi.org/10.3390/molecules26164880
17. Aqil, F., Ahmed, I., & Mehmood, Z. (2006). Antioxidant and antimicrobial activities of unavailable phenolic compounds isolated from *Lantana camara* L. leaves. *Journal of Agricultural and Food Chemistry*, 54(15), 5720–5726. https://doi.org/10.1021/jf060399g
18. Singh, R., & Sharma, R. (2022). Phytochemical screening and antioxidant potential of *Lantana camara* leaf extract. *Journal of Applied Pharmaceutical Science, 12*(3), 103–110. **https://doi.org/10.7324/JAPS.2022.120314**

19. Rao, M., & Shetty, J. (2022). Phytochemical screening and antioxidant activity of ethanolic extracts of *Lantana camara* leaves. *International Journal of Pharmaceutical Sciences Review and Research, 72*(1), 108–114. **https://doi.org/10.47583/ijpsrr.2022.v72i01.020**
20. Kokate, C. K., Purohit, A. P., & Gokhale, S. B. (2010). *Pharmacognosy* (45th ed.). Nirali Prakashan.
21. Pisoschi, A. M., Pop, A., Cimpeanu, C., & Predoi, G. (2016). Determination of the total antioxidant capacity and phytochemical screening in medicinal plants and natural products. *Journal of Analytical Methods in Chemistry, 2016*, 5377070. **https://doi.org/10.1155/2016/5377070**
22. Dhatwalia, B., & Sharma, N. (2024). Anti-oxidant and anti-cancerous properties of *Lantana camara* against mcf-7-in vitro .*Journal of Ayurveda & Holistic Medicine, 12*(2), 19-29. **https://www.wisdomlib.org/uploads/journals/jahm/volume-12-issue-2-2024/1277-824-2744.pdf**
23. Banik, U., & Islam, M. A. (2021). Application of ANOVA and post-hoc analysis to evaluate anticancer efficacy of natural products. *Biomedical Research and Therapy, 8*(12), 4631–4638. **https://doi.org/10.15419/bmrat.v8i12.706**
24. Dhatwalia B, Sharma N (2024) Phytochemical analysis of phenolic compounds by using LCMS of *Urginea indica*. *Journal of Ayurveda & Holistic Medicine.* 12(5):30–40. **https://jahm.co.in/index.php/jahm/article/view/1374**
25. Kim, S., Chen, J., Cheng, T., et al. (2021). PubChem 2023 update. *Nucleic Acids Research*, 51(D1), D1373–D1380.
26. Daina, A., Michielin, O., & Zoete, V. (2019). SwissTargetPrediction: Updated data and new features for efficient prediction of protein targets of small molecules. *Nucleic Acids Research*, 47(W1), W357–W364.
27. Stelzer, G., Plaschkes, I., Rozenberg, S., et al. (2016). The GeneCards suite: From gene data mining to disease genome sequence analyses. *Current Protocols in Bioinformatics*, 54, 1.30.1–1.30.33.
28. Szklarczyk, D., Gable, A. L., Lyon, D., et al. (2019). STRING v11: Protein–protein association networks with increased coverage, supporting functional discovery in genome-wide experimental datasets. *Nucleic Acids Research*, 47(D1), D607–D613.
29. Kohl, M., Wiese, S., & Göhring, B. (2011). Cytoscape: Software for visualization and analysis of biological networks. In *Data Mining in Proteomics* (pp. 291–303). Humana Press.
30. Ge, S. X., Jung, D., & Yao, R. (2020). ShinyGO: A graphical enrichment tool for animal model systems biology. *Bioinformatics*, 36(8), 2628–2629.
31. Dong, J., Cao, D. S., Miao, H. Y., et al. (2018). ChemDes: An integrated web-based platform for molecular descriptor and fingerprint computation. *Journal of Cheminformatics*, 7(1), 60.
32. Friesner, R. A., Murphy, R. B., Repasky, M. P., et al. (2006). Extra precision glide: Docking and scoring incorporating a model of hydrophobic enclosure. *Journal of Chemical Information and Modeling*, 46(6), 1657–1672.

33. Tuccinardi, T. (2021). Protein–ligand docking studies: A useful tool for medicinal chemistry. In *Computational Methods in Drug Discovery and Design* (pp. 215–238). Humana Press.
34. Albakova, Z. (2024). HSP90 multi-functionality in cancer. *Frontiers in Immunology, 15*, Article 1436973. https://doi.org/10.3389/fimmu.2024.1436973
35. Chatterjee, S., & Burns, T. F. (2017). Targeting heat shock proteins in cancer: A promising therapeutic approach. *International Journal of Molecular Sciences, 18*(9), Article 1978. https://doi.org/10.3390/ijms18091978
36. Daina, A., Michielin, O., & Zoete, V. (2019). SwissTargetPrediction: Updated data and new features for efficient prediction of protein targets of small molecules. *Nucleic Acids Research, 47*(W1), W357–W364. https://doi.org/10.1093/nar/gkz382
37. Dong, J., Wang, N. N., Yao, Z. J., Zhang, L., Cheng, Y., Ouyang, D., Lu, A. P., & Cao, D. S. (2018). ADMETlab: A platform for systematic ADMET evaluation based on a comprehensively collected ADMET database. *Journal of Cheminformatics, 10*, Article 29. https://doi.org/10.1186/s13321-018-0283-x
38. Friesner, R. A., Murphy, R. B., Repasky, M. P., Frye, L. L., Greenwood, J. R., Halgren, T. A., Sanschagrin, P. C., & Mainz, D. T. (2006). Extra precision glide: Docking and scoring incorporating a model of hydrophobic enclosure for protein-ligand complexes. *Journal of Medicinal Chemistry, 49*(21), 6177–6196. https://doi.org/10.1021/jm051256o
39. Kamal, A., Boehm, M. F., & Burrows, F. J. (2004). Therapeutic and diagnostic implications of Hsp90 activation. *Trends in Molecular Medicine, 10*(6), 283. https://doi.org/10.1016/j.molmed.2004.04.006
40. Kim, S., Chen, J., Cheng, T., Gindulyte, A., He, J., He, S., Li, Q., Shoemaker, B. A., Thiessen, P. A., Yu, B., Zaslavsky, L., Zhang, J., & Bolton, E. E. (2021). PubChem in 2021: New data content and improved web interfaces. *Nucleic Acids Research, 49*(D1), D1388–D1395. https://doi.org/10.1093/nar/gkaa971
41. Kiraly, S., Stanley, J., & Eden, E. R. (2025). Lysosome-mitochondrial crosstalk in cellular stress and disease. *Antioxidants, 14*(2), Article 125. https://doi.org/10.3390/antiox14020125
42. Kohl, M., Wiese, S., & Warscheid, B. (2011). Cytoscape: Software for visualization and analysis of biological networks. *Methods in Molecular Biology, 696*, 291–303. https://doi.org/10.1007/978-1-60761-987-1_18
43. Li, J., Han, X., Sun, M., Li, W., Yang, G., Chen, H., Guo, B., Li, J., Li, X., & Wang, H. (2023). Caspase-9 inhibition triggers Hsp90-based chemotherapy-mediated tumor intrinsic innate sensing and enhances antitumor immunity. *Journal for ImmunoTherapy of Cancer, 11*(12), Article e007625. https://doi.org/10.1136/jitc-2023-007625
44. Liu, R., Chen, Y., Liu, G., Li, C., Song, Y., Cao, Z., Li, W., Hu, J., Lu, C., & Liu, Y. (2020). PI3K/AKT pathway as a key link modulates the multidrug resistance of cancers. *Cell Death & Disease, 11*(9), Article 797. https://doi.org/10.1038/s41419-020-02998-6
45. Palabiyik, A. A. (2025). The role of Bcl-2 in controlling the transition between autophagy and apoptosis (Review). *Molecular Medicine Reports, 32*(1), Article 13537. https://doi.org/10.3892/mmr.2025.13537

46. Ploumaki, I., Triantafyllou, E., Koumprentziotis, I. A., Karampinos, K., Drougkas, K., Karavolias, I., Trontzas, I., & Kotteas, E. A. (2023). Bcl-2 pathway inhibition in solid tumors: A review of clinical trials. *Clinical and Translational Oncology, 25*(6), 1554–1578. https://doi.org/10.1007/s12094-022-03070-9
47. Qian, S., Wei, Z., Yang, W., Huang, J., Yang, Y., & Wang, J. (2022). The role of BCL-2 family proteins in regulating apoptosis and cancer therapy. *Frontiers in Oncology, 12*, Article 985363. https://doi.org/10.3389/fonc.2022.985363
48. Stelzer, G., Rosen, N., Plaschkes, I., Zimmerman, S., Twik, M., Fishilevich, S., Iny Stein, T., Nudel, R., Lieder, I., Mazor, Y., Kaplan, S., Dahary, D., Warshawsky, D., Guan-Golan, Y., Kohn, A., Rappaport, N., Safran, M., & Lancet, D. (2016). The GeneCards suite: From gene data mining to disease genome sequence analyses. *Current Protocols in Bioinformatics, 54*(1), 1.30.1–1.30.33. https://doi.org/10.1002/cpbi.5
49. Szklarczyk, D., Gable, A. L., Lyon, D., Junge, A., Wyder, S., Huerta-Cepas, J., Simonovic, M., Doncheva, N. T., Morris, J. H., Bork, P., Jensen, L. J., & von Mering, C. (2019). STRING v11: Protein–protein association networks with increased coverage, supporting functional discovery in genome-wide experimental datasets. *Nucleic Acids Research, 47*(D1), D607–D613. https://doi.org/10.1093/nar/gky1131
50. Tesoriere, A., Dinarello, A., & Argenton, F. (2021). The roles of post-translational modifications in STAT3 biological activities and functions. *Biomedicines, 9*(8), Article 956. https://doi.org/10.3390/biomedicines9080956
51. Tuccinardi, T. (2021). What is the current value of MM/PBSA and MM/GBSA methods in drug discovery? *Expert Opinion on Drug Discovery, 16*(11), 1233–1237. https://doi.org/10.1080/17460441.2021.1942836
52. Vogler, M., Braun, Y., Smith, V. M., Westhoff, M. A., Pereira, R. S., Pieper, N. M., Anders, M., Callens, M., Vervliet, T., Abbas, M., Macip, S., Schmid, R., Bultynck, G., & Dyer, M. J. S. (2025). The BCL2 family: From apoptosis mechanisms to new advances in targeted therapy. *Signal Transduction and Targeted Therapy, 10*(1), Article 91. https://doi.org/10.1038/s41392-025-02176-0
53. Ye, L., Ngan, D. K., Xu, T., Liu, Z., Zhao, J., Sakamuru, S., Zhang, L., Zhao, T., Xia, M., Simeonov, A., & Huang, R. (2022). Prediction of drug-induced liver injury and cardiotoxicity using chemical structure and in vitro assay data. *Toxicology and Applied Pharmacology, 454*, Article 116250. https://doi.org/10.1016/j.taap.2022.116250
54. Zhang, J., Li, H., Liu, Y., Zhao, K., Wei, S., Sugarman, E. T., Liu, L., & Zhang, G. (2022). Targeting HSP90 as a novel therapy for cancer: Mechanistic insights and translational relevance. *Cells, 11*(18), Article 2778. https://doi.org/10.3390/cells11182778
55. Aits S, Jäättelä M (2023) Lysosomal control of cell death and survival. *Nat Rev Mol Cell Biol* 24:567–586
56. Wang F, et al (2021) Cathepsin-mediated mitochondrial apoptosis in cancer. *Cell Death Dis* 12:1063
57. Frank DA, et al (2020) STAT3 oncogenic signaling in cancer. *Cancer Res* 80:2457–2467

58. Thorpe LM, Yuzugullu H, Zhao JJ (2020) PI3K–AKT signaling in cancer. *Nat Rev Cancer* 20:233–249
59. Lee HH, et al (2021) EGFR–AKT–STAT3 signaling regulates BCL-2 expression in epithelial cancers. *Oncogene* 40:2765–2778
60. Julien O, Wells JA (2020) Caspases and their substrates. *Cell Death Differ* 27:240–252
61. Brentnall M, et al (2022) Executioner caspase activation in cancer cell death. *Cancers* 14:1859
62. Daina A, Michielin O, Zoete V (2020) SwissADME: a free web tool for pharmacokinetics. *Sci Rep* 10:11029
63. Ferreira LL, et al (2023) In silico ADMET profiling in drug discovery. *Drug Discov Today* 28:103401